Applied Catalysis B: Environmental 144 (2014) 614–621

Contents lists available at ScienceDirect

Applied Catalysis B: Environmental

journal homepage: www.elsevier.com/locate/apcatb

Visible light-sensitized S, N and C co-doped polymorphic TiO_2 for photocatalytic destruction of microcystin-LR

Geshan Zhang[a], Yong Cai Zhang[b], Mallikarjuna Nadagouda[c], Changseok Han[a], Kevin O'Shea[d], Said M. El-Sheikh[e], Adel A. Ismail[e], Dionysios D. Dionysiou[a,*]

[a] Environmental Engineering and Science Program, University of Cincinnati, Cincinnati, OH 45221, United States
[b] College of Chemistry and Chemical Engineering, Yangzhou University, Yangzhou 225002, PR China
[c] US EPA, National Risk Management Research Laboratory, Cincinnati, OH 45268, United States
[d] Department of Chemistry and Biochemistry, Florida International University, Miami, FL 33199, United States
[e] Central Metallurgical R&D Institute, Cairo 11421, Egypt

ARTICLE INFO

Article history:
Received 25 April 2013
Received in revised form 12 July 2013
Accepted 26 July 2013
Available online 7 August 2013

Keywords:
S, N and C co-doped polymorphic TiO_2
Sol–gel method
Thiourea
Visible light-sensitized
Microcystin-LR

ABSTRACT

Motivated from the increasing environmental concerns associated with the formation of cyanotoxins released by cyanobacteria in waters, this study focused on the synthesis and evaluation of visible light-sensitized S, N and C co-doped polymorphic titanium dioxide (CDPM-TiO_2) nanoparticles for photocatalytic destruction of microcystin-LR, one of the most common and toxic cyanotoxins. The CDPM-TiO_2, containing anatase, brookite and rutile phase, was synthesized using a modified sol–gel method followed by calcination at 300—600 °C. Thiourea was utilized as a precursor for the dopants. This work took the initiative to have detailed characterization on the co-doped polymorphic TiO_2 by several techniques and utilize the CDPM-TiO_2 on cyanotoxin treatment. The results showed that the physicochemical properties of CDPM-TiO_2 samples were highly dependent on the calcination temperature. The CDPM-TiO_2 sample calcined at 300 °C (CDPM300) exhibited better physicochemical characters including higher surface area and stronger photo-absorption in the visible light region. The sulfur dopant was attributed to S^{6+} species; nitrogen was ascribed to interstitial N; carbon was assigned to the Ti—O—C bond. Moreover, CDPM300 showed highest photocatalytic activity for microcystin-LR destruction under visible light irradiation among all CDPM-TiO_2 nanoparticles, which can be considered as a promising demonstration of such visible light-sensitized photocatalysts in the treatment of an important cyanotoxin in water.

1. Introduction

Cyanobacteria (blue-green algae) blooms have been a significant concern to public health and the environment because they can produce and release hepatotoxic, cytotoxic and/or neurotoxic cyanotoxins into fresh waters, several of which serve as the sources of drinking water supplies [1]. The most well-known cyanotoxin family is that of the monocyclic heptapeptide microcystins (MCs) which consist of more than 90 variants [2]. Microcystin-LR (M.W. = 995.2 g/mol) is generally considered as the most widespread and toxic MC congener and is the only cyanotoxin for which a provisional guideline value of 1 μg/l in drinking water has been proposed by the World Health Organization (WHO) [3,4]. Microcystin-LR has strong hepatotoxicity and can cause inhibition of protein phosphatases 1 and 2A [5,6]. Many reports have shown that even at low concentrations chronic microcystin-LR exposure can induce liver cancer [5–7]. Therefore, effective treatment of microcystin-LR and other cyanotoxins in fresh waters, especially in those that serve as sources of drinking water supply, is of extreme importance for public health and environmental safety.

However, microcystin-LR and other cyanotoxins cannot always be efficiently removed by conventional water treatment processes [8,9]. Several emerging treatment processes, including the so-called advanced oxidation technologies (AOTs), are being explored as alternative or complementary approaches to conventional processes. Among such AOTs, titanium dioxide (TiO_2) photocatalysis has been intensively studied and demonstrated to be an effective alternative for the destruction of microcystins in water [1,10–12]. However, conventional TiO_2 photocatalyst can only utilize the light with wavelengths shorter than 388 nm (UV range) due to its wide band gap (e.g. $E_g \approx 3.2$ eV for anatase), which limits its application with solar light. Many efforts have been made in the last two

* Corresponding author at: Environmental Engineering and Science Program, University of Cincinnati, Cincinnati, OH 45221, United States. Tel.: +1 513 556 0724; fax: +1 513 556 4162.
E-mail address: dionysios.d.dionysiou@uc.edu (D.D. Dionysiou).

0926-3373/$ – see front matter © 2013 Elsevier B.V. All rights reserved.
http://dx.doi.org/10.1016/j.apcatb.2013.07.058

decades in order to overcome this limitation. Two main approaches are dye sensitization [13,14] and doping with impurities. In the approaches dealing with doping impurities, transition metals (Fe, Co, Ag or Ni) [15] or non-metals (N, F, S or C) [16–19] were utilized as dopants to narrow the band gap (or form intra band gap [20]) of TiO_2 materials and decrease the required activation energy. However, due to some drawbacks of metal-doped TiO_2 (such as potential metal leaching and photocorrosion) the non-metal-doped process is considered as a more environmentally-friendly and effective approach [16]. Nitrogen-doped TiO_2 can achieve band gap narrowing through either the mixing of nitrogen 2p states with oxygen 2p states on the top of the valence band at substitutional lattice sites or the generation of inter-gap states induced by formation of NO bond with the π character at interstitial lattice sites [21]. In the case of sulfur doping, sulfur substitutes either the oxygen as an anion or the titanium as a cation [22]. The overlap of sulfur 3p states and oxygen 2p states facilitates the visible light catalytic activity of S-doped TiO_2 [23]. For low concentration carbon impurities, Di Valentin et al. have reported that carbon atoms prefer to be interstitial and substitutional to Ti atoms under oxygen-rich conditions, whereas they prefer to be substitutional to O under anoxic conditions [24]. Among non-metal-doped TiO_2 materials, co-doped TiO_2 usually shows higher photocatalytic activity in the visible range because of the merits benefited from each dopant [16]. Most of the doped matrices are single anatase phase TiO_2 due to its high activity [25]. However, research has shown some polymorphic TiO_2 (e.g. Degussa P25) exhibited higher activity [26–28]. To the best of our knowledge, only a few research studies have dealt with visible light-activated polymorphic titania containing anatase, brookite and rutile phase [29,30]. Studies on S, N and C co-doped polymorphic TiO_2 as well as its photocatalytic activity have not been reported so far. It is hypothesized that such materials will have increased performance under visible light because of the possibility of sensitization by various mid gap energy sensitization levels introduced by the various non-metals as well as better electron–hole separation due to the formation of heterojunctions. Moreover, minimum information is available on the application of co-doped polymorphic TiO_2 for cyanotoxin destruction under visible light.

In the present work, visible light-sensitized S, N and C co-doped TiO_2 nanoparticles (CDPM-TiO_2), containing brookite, anatase and rutile phases, were synthesized with a modified sol–gel method [31,32] followed by calcination of the resulting materials at higher temperatures (300—600 °C). Thiourea was applied as a source of the dopants. The CDPM-TiO_2 was characterized with X-ray diffraction (XRD), Raman, porosimetry analysis, high resolution transmission electron microscopy (HR-TEM), UV-vis diffuse reflectance spectroscopy (DRS), X-ray photoelectron spectroscopy (XPS) and Fourier transform infrared (FT-IR) spectroscopy. The photocatalytic destruction of microcystin-LR by CDPM-TiO_2 nanoparticles was evaluated under visible light. The effects of calcination temperature and adding sequence of doping precursor were investigated to optimize the conditions for obtaining CDPM-TiO_2 with the highest visible light photocatalytic activity for microcystin-LR degradation.

2. Experimental

2.1. Preparation of CDPM-TiO_2 nanoparticle

To synthesize CDPM-TiO_2 nanoparticles, titanium tetrachloride ($TiCl_4$, ≥99.0%, Fluka, 0.1 M in final solution) was selected as the Ti precursor, which was added into concentrated hydrochloric acid (HCl, 37.3%, Fisher, 0.3 M in final solution) and mixed with Milli-Q water (Millipore Corp., Billerica, MA) and isopropanol (99.8%, Pharmco-Aaper). The ratio of Milli-Q water to isopropanol was 1:2 (v/v). Thiourea (Fisher, 5% molar ratio of Ti) was added to the reaction solution and dissolved before heating. The above mixture was heated and refluxed at 85 °C for 15 h in an oil bath under magnetic stirring. After cooling down, the mixture was transferred to petri dishes and dried at room temperature for 48 h. The above procedure was mainly based on the work of Lee et al. [31,32]. After drying, the obtained powders were then calcined at different temperatures (300—600 °C) for 2 h in a multi-segment programmable high temperature furnace (Paragon Model HT-22-D, Thermcraft Inc., Winston-Salem, NC). After cooling down, the calcined powders were washed with Milli-Q water and isopropanol for three times to remove any organic or inorganic residues. Before photocatalytic experiment, the powders were dried, ground, and dispersed in Milli-Q water by using an ultrasonicator (2510R-DH, Bransonic). For reference "Blank", no thiourea was added during the synthesis and did not apply calcination; for "Blank300", no thiourea was added during the synthesis but applied calcination at 300 °C for 2 h.

2.2. Characterization of CDPM-TiO_2 nanoparticle

The physicochemical properties of CDPM-TiO_2 were characterized by XRD, HR-TEM, XPS, Raman, FT-IR, porosimetry analysis and DRS. XRD analysis for synthesized CDPM-TiO_2 nanoparticles was performed on a PANalytical Xpert Pro theta-two theta diffractometer with Cu Kα radiation at 45 kV and 40 mA (λ = 1.5406 Å) in order to identify the crystal phase and determine the primary crystallite size. The BET surface area and pore size distribution for CDPM-TiO_2 nanoparticles were measured using a Tristar 3000 porosimeter analyzer (Micromeritics). Raman analysis was carried out on a Renishaw InVia Raman spectrometer using a high power near infrared (Near-IR) diode laser (λ = 785 nm, 500 mW) as the excitation source. A HR-TEM (JEM-2010F, JEOL) with a field emission-transmission gun at 200 kV was utilized to investigate the morphology and crystallinity of the samples. For HR-TEM sample preparation, the particles were dispersed in Milli-Q water by ultrasonication for more than 15 min and fixed on a carbon-coated copper grid (FCF400-Cu, EMS). A UV-vis spectrophotometer (UV-2501 PC, Shimadzu) with an integrating sphere attachment (ISR 1200) was applied for diffuse reflectance measurements to investigate the optical properties and band gap of CDPM-TiO_2 nanoparticles. $BaSO_4$ was used as the reference. Bruker Tensor 27 FT-IR spectrometer was employed to detect the doping groups on the CDPM-TiO_2 samples. The FTIR spectra were analyzed at room temperature with samples in a KBr wafer. For the surface properties and elemental composition of CDPM-TiO_2 particles, XPS measurements were conducted by Thermo-VG Scientific ESCALAB 250 XPS system with Al Kα X-ray radiation. The binding energies were corrected by C 1s level at 284.6 eV as a reference to reduce the relative surface charging effect.

2.3. Photocatalytic experiments

To examine the photocatalytic activities of CDPM-TiO_2 nanoparticles, the experiments for microcystin-LR destruction were conducted under visible light irradiation. The photocatalytic reaction was performed in a borosilicate glass Petri dish (Pyrex, 60 mm (ø) × 15 mm (h)) sealed with a quartz cover and cooled with fans to avoid solution evaporation. Microcystin-LR (99.3%, Cal-Biochem) stock solution was spiked in Milli-Q water (pH = 5.7) to achieve an initial concentration of 0.5 μM. The synthesized CDPM-TiO_2 samples (0.5 g/l) applied in the reaction were prepared as suspensions with ultrasonication. The final volume of the reaction solution was 10.0 ml. Two 15 W fluorescent lamps (Cole-Parmer) with a UV block filter (UV420, Opticology) [18] were applied as the visible light source and the light intensity was 1.33 mW/cm^2 which was determined with a radiant power

Table 1
Phase content and preparation parameters of CDPM-TiO_2 samples and reference materials.

	Sample ID	Thiourea adding	Calcination temperature	Phase content fraction (wt.%)		
				Anatase	Brookite	Rutile
Reference samples	Blank	Not applied	Not applied	61.5	30.1	8.4
	Blank300	Not applied	300 °C	54.0	38.6	7.5
CDPM-TiO_2 samples	ES_CDPM300	5% after the oil bath synthesis	300 °C	55.1	37.9	7.0
	CDPM300	5% at beginning	300 °C	59.5	34.3	6.2
	CDPM400	5% at beginning	400 °C	54.9	37.1	7.9
	CDPM500	5% at beginning	500 °C	42.7	36.8	20.4
	CDPM600	5% at beginning	600 °C	23.3	10.2	66.5

meter (Newport Corp.). The solution in the reactor was irradiated under the visible light with continuous stirring. 0.2 ml samples were taken after 0, 1, 2, 3, 4 and 5 h, diluted with 0.2 ml methanol, and filtered with 0.2 μm syringeless filters (PTFE, Whatman). The destruction of microcystin-LR with irradiation time was monitored through the quantification of microcystin-LR by using a high-performance liquid chromatograph (HPLC, Series 1100, Agilent) with a photodiode-array detector (PDA) set at 238 nm. A C_{18} Discovery HS (Supelco) column (150 mm × 2.1 mm, 5 μm particle size) was employed as the stationary phase and the mobile phase was 0.05% (v/v) trifluoroacetic acid (101.7%, TFA, Fisher) in Milli-Q water and 0.05% TFA in acetonitrile (99.9%, Tedia) in a ratio of 60:40. The analysis was performed under equilibrium conditions with a column temperature of 40 °C, a flow rate of 0.2 ml/min and an injection volume of 20 μl [33]. The photocatalytic experiments for each catalyst were carried out in triplicates.

3. Results and discussion

3.1. Physicochemical characteristics of CDPM-TiO_2 nanoparticle

In this work, five CDPM-TiO_2 nanoparticle samples and two reference samples were synthesized by the procedures mentioned in Section 2.1. The preparation parameters of each sample are listed in Table 1. Unlike other CDPM-TiO_2 samples (in situ doping), sample ES_CDPM300 was prepared through an ex situ doping process in which the thiourea was not added at the beginning but after the oil bath synthesis. Fig. 1 shows the XRD patterns of CDPM-TiO_2 and reference samples. The diffraction peaks corresponding to the anatase, brookite and rutile phase were identified in each XRD pattern of different samples. According to the work of Zhang and Banfield [34], the phase content of a polymorphic TiO_2 sample can be calculated from the integrated intensities of anatase (1 0 1), brookite (1 2 1) and rutile (1 1 0) peaks. The phase contents of different CDPM-TiO_2 nanoparticles through calculation are shown in Table 1. When the calcination temperature was lower than 400 °C, the content of anatase phase in CDPM-TiO_2 samples as well as sample Blank300 was stable in the range of 54—60%. The content was 34—39% for brookite phase and 6—8% for rutile phase. The lattice spacing of each phase (D(1 0 1), D(1 2 1) or D(1 1 0)) of all samples had no significant difference (±0.02 Å) based on Bragg's law. By comparing the atom radius of sulfur (1.00 Å), nitrogen (0.65 Å) and carbon (0.7 Å) to that of oxygen (0.60 Å) and titanium (1.40 Å), the relatively small variation on lattice spacing (±0.02 Å) suggests the insignificant change of crystal structure in CDPM-TiO_2 samples which is probably due to the low doping percentage.

Under the experimental conditions applied in this study, higher calcination temperature generally resulted in lower anatase phase fraction, higher rutile phase fraction, and sharper diffraction peaks indicating larger crystal size (see Table 2) and higher crystallinity. Among the CDPM-TiO_2 samples, CDPM300 exhibited the smallest crystal size, as determined on the basis of the Scherrer equation and diffraction peaks of anatase (1 0 1), brookite (1 2 1) and rutile (1 1 0), which suggests more catalytic active surface sites per unit catalyst mass [35]. Consequently, CDPM300 was expected to have the highest surface area, which was proved by a BET surface area measurement with S_{BET} of 136 m^2/g. The nitrogen adsorption–desorption isotherms of CDPM-TiO_2 samples, shown in Fig. 2(a), belong to type IV which is typical for mesoporous materials. Based on the BJH pore size distribution data (Fig. 2(b)), CDPM300 and ES_CDPM300 had very narrow distribution of 2—6 nm. Higher calcination temperatures (400—600 °C) resulted in larger pore sizes and broader pore size distributions but in smaller pore volumes and lower porosities listed in Table 2. Interestingly, CDPM300 sample displayed a main peak at the pore size of 2.9 nm along with a shoulder peak at the pore size of around 3.7 nm, indicating its special bimodal pore structure.

The CDPM-TiO_2 samples and reference materials were also characterized by Raman spectroscopy (displayed in Fig. 3) for their structure properties. The results of Raman analysis are consistent with the XRD results that all samples are polymorphic TiO_2 [36,37] whose phase content (anatase, brookite and rutile) varies with

Table 2
Characteristics of CDPM-TiO_2 samples and reference materials.

Sample ID	Anatase		Brookite		Rutile		S_{BET} (m^2/g)	Pore volume (m^3/g)	Porosity (%)[e]
	Crystal size (nm)[a]	D(1 0 1) (Å)[b]	Crystal size (nm)[a]	D(1 2 1) (Å)[c]	Crystal size (nm)[a]	D(1 1 0) (Å)[d]			
Blank	5.2	3.50	7.6	2.90	12.0	3.26	165.2	0.108	30.1
Blank300	6.7	3.49	8.7	2.91	17.2	3.24	108.8	0.111	30.8
ES_CDPM300	6.7	3.49	7.9	2.89	12.7	3.23	123.0	0.106	29.8
CDPM300	6.4	3.47	7.8	2.88	12.7	3.24	135.9	0.109	30.3
CDPM400	8.0	3.49	9.7	2.89	17.8	3.24	85.6	0.087	25.8
CDPM500	10.2	3.49	11.0	2.88	21.9	3.23	35.5	0.055	18.2
CDPM600	17.1	3.50	15.1	2.88	28.3	3.23	12.3	0.035	12.7

[a] Based on XRD analysis, using the Scherrer equation: crystal size = $0.9\lambda/(\beta \times \cos\theta)$, where $\lambda = 0.154$ nm, θ is the Bragg angle, and β is the full wide at half the maximum intensity (FWHM).
[b,c,d] Based on XRD analysis by using Bragg's law: lattice spacing $(D) = \lambda/(2 \times \sin\theta)$.
[e] Porosity (%) = pore volume (cm^3/g)/(pore volume (cm^3/g) + solid TiO_2 volume without pore (cm^3/g)) × 100%; solid TiO_2 volume without pore (cm^3/g) = 1/density of the solid TiO_2 without pore, based on phase content and anatase (3.88 g/cm^3), brookite (4.13 g/cm^3) and rutile (4.23 g/cm^3) density.

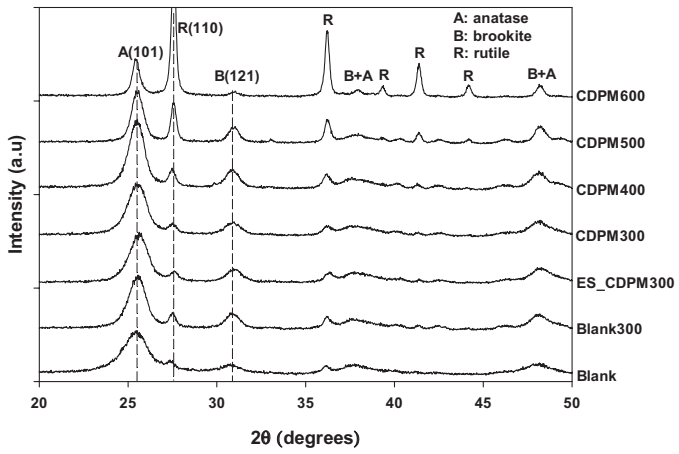

Fig. 1. XRD patterns of CDPM-TiO_2 nanoparticles.

synthesis conditions. The Raman peak shifts of 144 cm^{-1} (E_g), 198 cm^{-1} (E_g), 397 cm^{-1} (B_{1g}), 516 cm^{-1} (A_{1g} and B_{1g}) and 639 cm^{-1} (E_g) are assigned to anatase phase; Raman shifts of 194 cm^{-1} (A_g), 215 cm^{-1} (B_{1g}), 247 cm^{-1} (A_g), 320 cm^{-1} (B_{1g}), 366 cm^{-1} (B_{2g}), 452 cm^{-1} (B_{3g}) and 640 cm^{-1} (A_g) belong to brookite phase; Raman shifts of 449 cm^{-1} (E_g) and 610 cm^{-1} (A_{1g}) are attributed to rutile phase [38]. Moreover, the main anatase

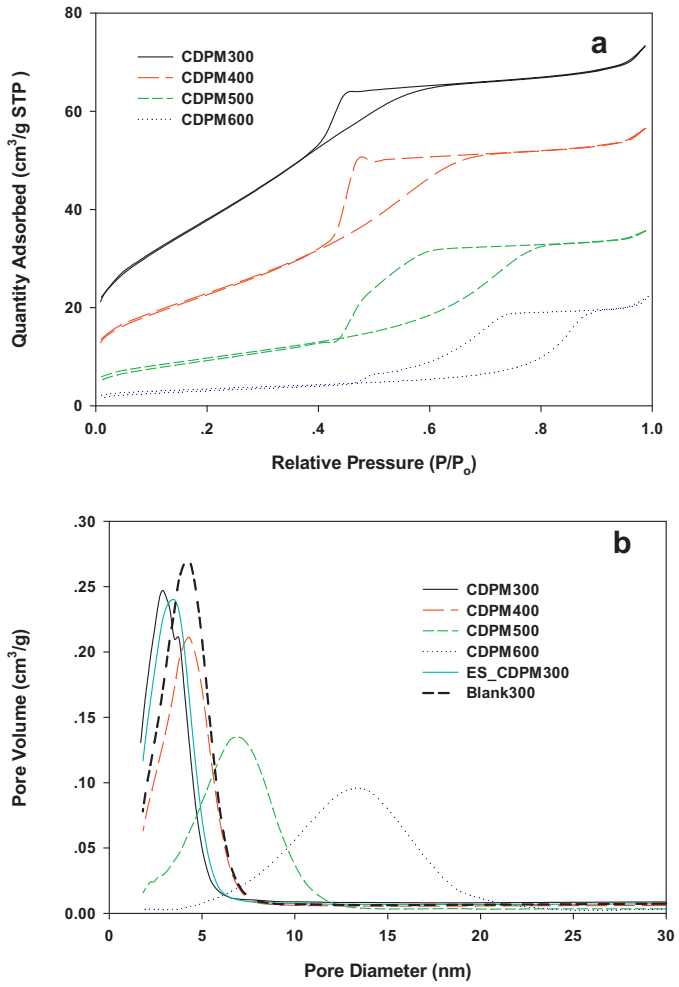

Fig. 2. (a) N_2 adsorption–desorption isotherms of CDPM-TiO_2 nanoparticles and (b) the pore size distribution of CDPM-TiO_2 nanoparticles and reference material.

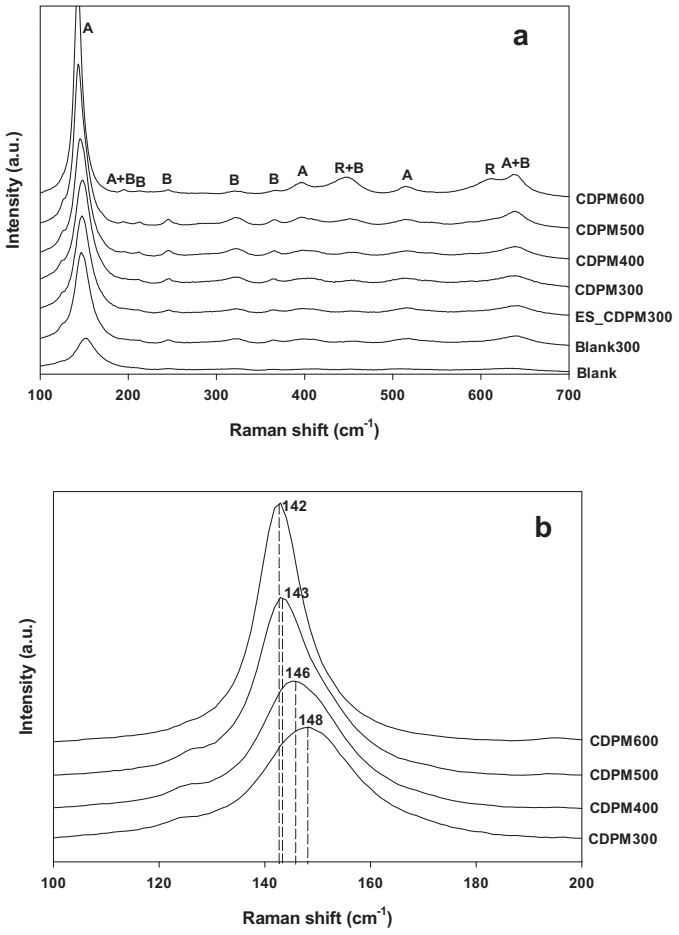

Fig. 3. (a) Raman spectra of CDPM-TiO_2 nanoparticles and reference material and (b) the main anatase Raman band of CDPM-TiO_2 samples.

Raman band (E_g mode, peak position at around 144 cm^{-1}) was sharpened and blue-shifted (see Fig. 3(b)) when a higher calcination temperature was applied. Other research studies [39–41] found that larger crystal size would bring sharper and more blue-shifted Raman band and attributed this phenomenon to the size confinement effect. In this research, higher calcination temperature resulted in a larger crystal size. Therefore, the size confinement effect is believed to be mainly responsible for Raman band shift and narrowing.

Fig. 4 shows the HR-TEM images of sample CDPM300. The diameter of CDPM300 nanoparticle was around 6—10 nm. The phase content of CDPM300 was confirmed by the selected area electron diffraction (SAED) pattern (the inset in Fig. 4(a)) as polymorph (anatase, brookite and rutile) TiO_2. Besides, the lattice spacings of anatase D(1 0 1), brookite D(1 2 1) and rutile D(1 1 0) were calculated as 0.347 nm, 0.288 nm and 0.324 nm, respectively, which are in agreement with the results calculated from XRD analysis. The fast Fourier transform (FFT, inset in Fig. 4(b)) pattern of the CDPM300 sample shows the anatase and brookite crystal phase. The lattice fringes also match the anatase and brookite phases of TiO_2. The D(1 0 1) of anatase shown in Fig. 4(c) is 0.351 nm and D(1 2 1) of brookite is 0.292 nm (Fig. 4(d)) which are also similar with the results from SAED pattern and XRD analysis. The lattice fringe of rutile (1 1 0) plane was not found in the HR-TEM images due to its low fraction in the sample.

The UV–vis absorption spectra of CDPM-TiO_2 samples and reference materials are shown in Fig. 5. The reference samples (Blank and Blank300) had no significant absorbance in the visible light region

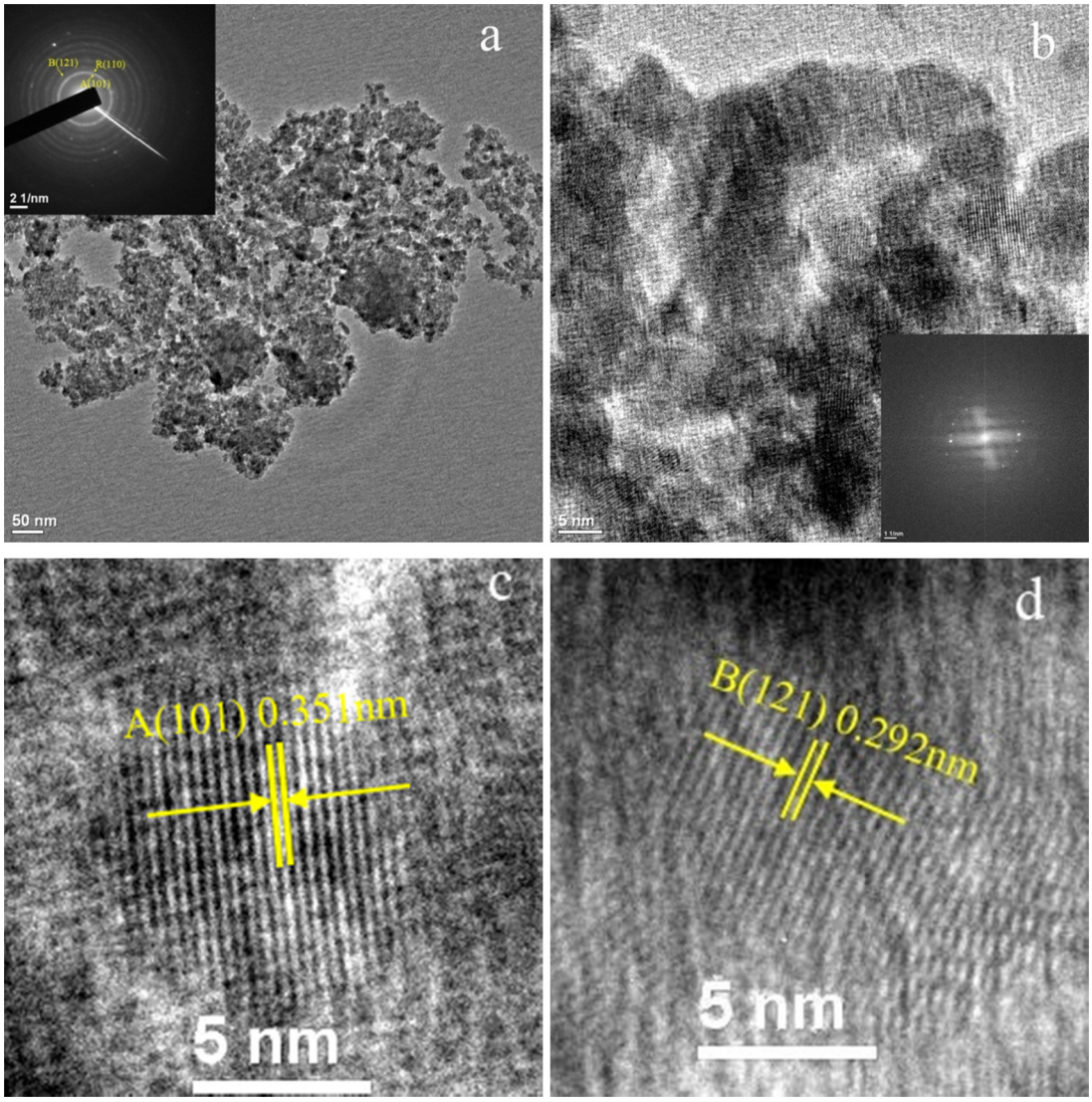

Fig. 4. HR-TEM images of CDPM300 nanoparticle. The inset in (a) shows its SAED pattern. The inset in (b) shows its FFT pattern.

($\lambda > 420$ nm). However, the absorption edges of all CDPM-TiO_2 samples were shifted to a lower energy region. The results indicated that the elements doped into TiO_2 lattice were responsible for the red-shift absorption band of CDPM-TiO_2 samples. Moreover, sample CDPM300 showed the strongest photo-absorption in the visible light region, which could imply promise for higher visible light photocatalytic activity. The visible light absorbance of CDPM-TiO_2 was lower when a higher calcination temperature was applied, which is in good agreement with several previous reports [18,42,43] and can be explained by the thermal release of doped non-metal elements at higher calcination temperature [44]. The band gap (E_g) was determined according to transformed Kubelka–Munk function (inset in Fig. 5), assuming indirect transition [45,46]. The E_g value of CDPM300 is 2.95 eV, which is lower than that of reference samples Blank (E_g = 2.99 eV) and Blank300 (E_g = 3.06 eV). The results demonstrate that doping can reduce the band gap of polymorphic titania and hence reduce the energy required for photoactivation.

In order to detect the nature of doped elements, the doped TiO_2 samples were also analyzed by XPS and FT-IR spectrometer (shown in Figs. 6 and 7). The S 2p XPS peak centered at 168.3 eV for both CDPM300 and ES_CDPM300 (Fig. 6(a)) can be attributed to S^{6+} species [22,42,47–49]. This is also consistent with the previous

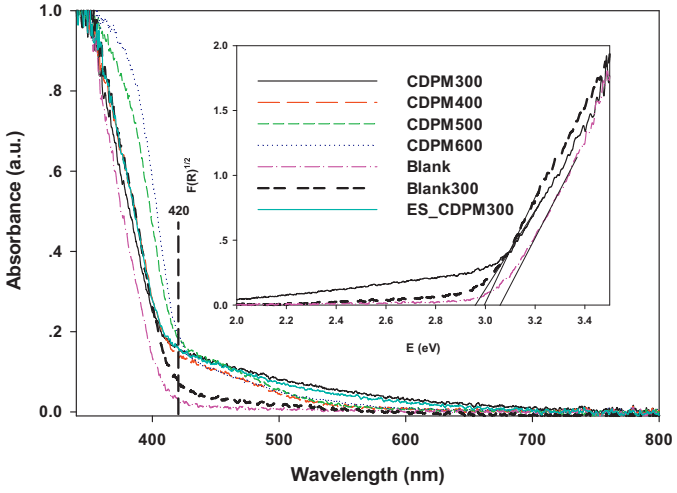

Fig. 5. UV–vis absorption spectra of CDPM-TiO_2 nanoparticles and reference materials. The inset displays the Tauc plots of modified Kubelka–Munk function.

reports that the substitution of Ti^{4+} by S^{6+} is much easier than the replacement of O^{2-} with S^{2-} [22]. The atomic content of sulfur in CDPM300 and ES_CDPM300 is 1.73% and 1.24%, respectively, which indicates more sulfur dopant is able to be doped in a TiO_2 sample through the in situ doping process. Our previous work [18] had demonstrated the thermal annealing process can annihilate the sulfur content. The N 1s XPS spectra show two constituent peaks at around 399.4 and 401.1 eV, without the peak at 396—397 eV definitely assigned to substitutional nitrogen. Meanwhile, peaks at around 400 eV were ascribed to interstitial nitrogen [21], which fits to the XPS data obtained in this work. The atomic content of nitrogen in CDPM300 is higher than that in ES_CDPM300. As displayed in Fig. 6(c), three constituents were found in C 1s XPS spectra of both samples at around 284.6, 286.0 and 288.4 eV. The peak at 284.6 eV can be assigned to hydrocarbons which arise from residue organics of the sample as well as adventitious carbon contamination in XPS measurement [50,51], whereas the peaks at 286.0 and 288.4 eV can be attributed to C—O bond and C═O (or O—C—O) bond, respectively [52–55]. The peak at 288.4 eV can suggest the substitution of Ti atom by C and formation of Ti—O—C structure [54,55]. The peak around 282 eV was not observed, indicating the absence of substitution of oxygen atom by carbon [52,54,55]. Since this work was conducted under oxygen-rich conditions, the above result is also consistent with the conclusion of Di Valentin et al. [24]. The results from FT-IR analysis further confirm the results and conclusion from XPS analysis (Fig. 7). The absorption peaks at 1130 cm^{-1} and 1048 cm^{-1} are assigned to Ti—O—S bond and Ti—S bond, respectively [18,56,57]. The weak band at 1410 cm^{-1} can be ascribed to the bending vibration of ammonium ion, while the absorption around 1580 cm^{-1} should be attributed to bidentate nitrate [58,59]. The band at 1381 cm^{-1} is most probably due to the methyl bending vibration from residual isopropanol [60]. The peak at 1627 cm^{-1} can be attributed to the bending vibration of O—H bond from surface adsorbed water [61]. The broad band around 590 cm^{-1} belongs to the Ti—O bending vibration [62].

3.2. Photocatalytic activity of CDPM-TiO_2 nanoparticle under visible light

The comparison of photocatalytic activity of S, N and C co-doped TiO_2 nanoparticles for microcystin-LR degradation under visible light irradiation is shown in Fig. 8. In the presence of CDPM300 particle, the highest removal of microcystin-LR (75%) was achieved within 5 h. CDPM-TiO_2 samples calcined above 300 °C showed lower photocatalytic activity. Fig. 8(b) shows the microcystin-LR degradation rates within the initial 2 h. The solid bars display the total removal of microcystin-LR including degradation and adsorption while the bars with strips show the result of microcystin-LR adsorption on the catalysts. Therefore, the initial 2 h removal rate caused by photocatalytic degradation with samples CDPM300, CDPM400, CDPM500 and CDPM600 can be calculated as 14.3×10^{-4}, 10.2×10^{-4}, 5.4×10^{-4} and 2.6×10^{-4} μM/min, respectively. The results indicate CDPM300 has the highest photocatalytic activity under visible light. Moreover, sample CDPM300 showed higher adsorption capacity which was expected due to its higher surface area. Hence the CDPM300 nanoparticle demonstrated higher removal efficiency for microcystin-LR due to both its higher visible light photocatalytic activity and greater adsorption capacity. While CDPM300 and CDPM400 had similar anatase, brookite and rutile phase fraction, the visible light photocatalytic activity of CDPM300 was 40% higher than that of CDPM400, which indicates that the higher dopants content in CDPM300 is the main reason for its higher photocatalytic activity here according to our previous work [18]. However, other studies showed nano-TiO_2 with an optimum polymorphic ratio would exhibit higher photocatalytic

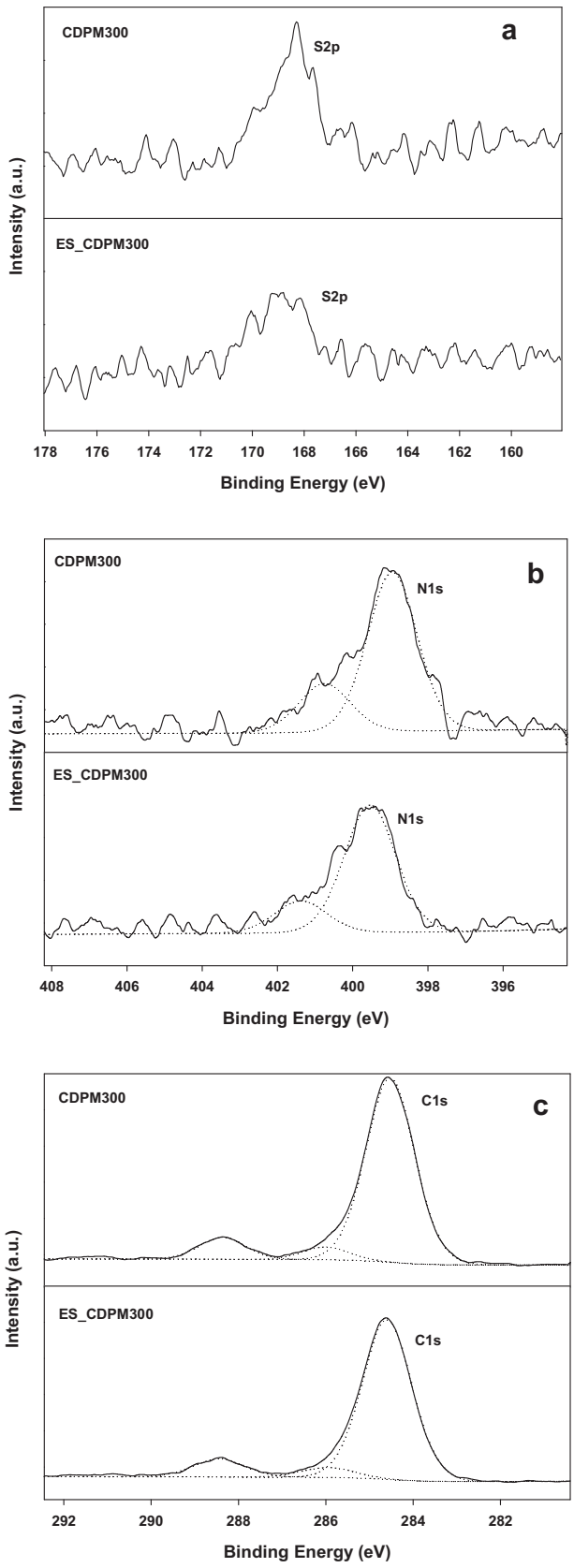

Fig. 6. XPS spectra of S 2p (a), N 1s (b) and C 1s (c) regions for sample CDPM300 and ES_CDPM300.

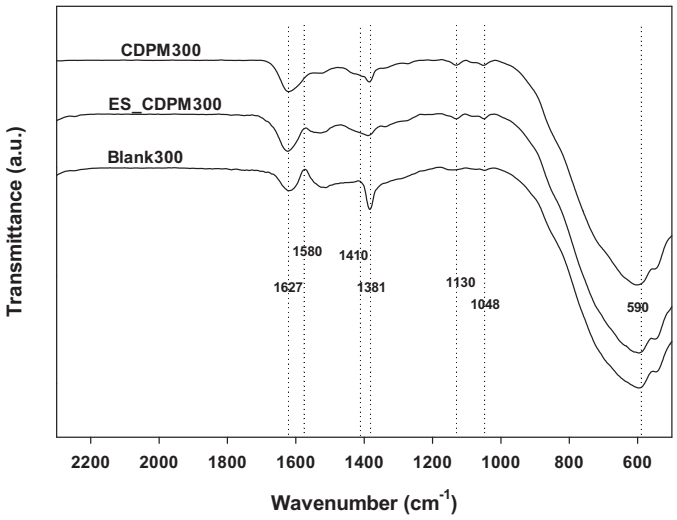

Fig. 7. FT-IR spectra of sample CDPM300, ES_CDPM300 and reference sample Blank300.

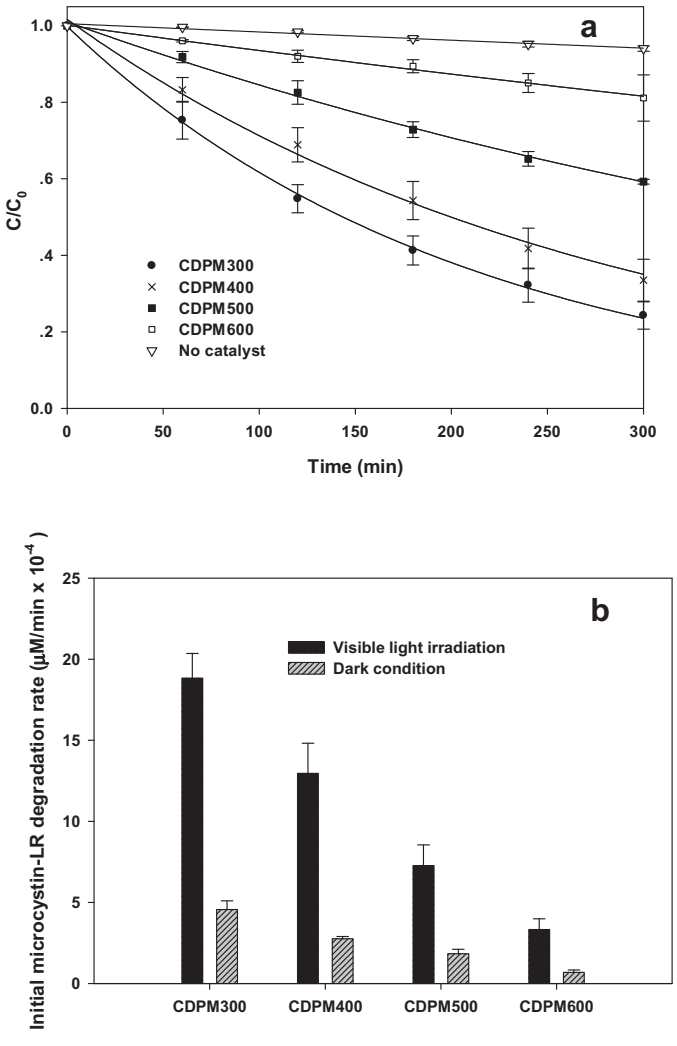

Fig. 8. (a) The visible light photocatalytic degradation of microcystin-LR with CDPM-TiO_2 nanoparticles and (b) the initial 2 h microcystin-LR degradation rates with different CDPM-TiO_2 samples.

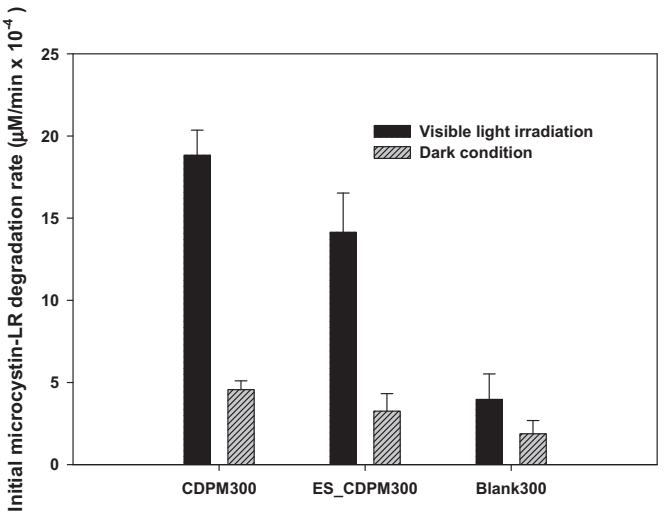

Fig. 9. The initial 2 h microcystin-LR degradation rate with different samples calcined at 300 °C.

activity [63,64]. Therefore, the polymorph contents may play a role in photocatalytic activity of CDPM-TiO_2 catalysts. Polymorphic TiO_2 with different polymorph contents but same dopant content can be investigated further in order to study the effect of polymorphic ratio.

Fig. 9 shows the summarized results of the initial 2 h microcystin-LR degradation rate with sample CDPM300 (in situ), ES_CDPM300 (ex situ) and Blank300 (reference) which were all calcined at 300 °C. The total removal of microcystin-LR as well as adsorption for the ES_CDPM300 sample were less than those for the CDPM300 sample, which should be attributed to the lower surface area and worse photocatalytic activity (calculated initial 2 h removal rate of 10.9×10^{-4} μM/min) of the ES_CDPM300 sample. Many other works have reported that a TiO_2 catalyst produced by an in situ process demonstrated better catalytic activity compared to materials produced by an ex situ method [65,66], which is in good agreement with the results obtained in this work. In this study, sample CDPM300 exhibited the highest photocatalytic activity under the experimental conditions applied herein, which can be attributed to the higher content of dopants, the more intra photoactive centers [20] and potentially the larger number of catalytic active surface sites per unit catalyst mass due to its higher surface area.

4. Conclusion

This study dealt with the synthesis of S, N and C co-doped polymorphic titanium dioxide nanoparticles (CDPM-TiO_2) for the photocatalytic destruction of microcystin-LR under visible light irradiation. According to the results from the characterization experiments, the physicochemical properties of CDPM-TiO_2 samples were highly dependent on the calcination temperature, which largely affected their crystal phase fraction, crystallinity, crystal size, surface area, pore size and pore size distribution. Among all CDPM-TiO_2 samples, CDPM300 (calcined at 300 °C) exhibited stronger photo-absorption in the visible light region and higher dopant content, which all indicate its potential for higher visible light photocatalytic activity. According to XPS and FT-IR spectra, sulfur was mainly attributed to S^{6+} species and can form a Ti—O—S bond; nitrogen was ascribed to interstitial N; carbon was assigned to the Ti—O—C bond in the CDPM-TiO_2 samples. CDPM300 showed the highest photocatalytic activity for microcystin-LR degradation under visible light irradiation. In addition, adding the dopants precursor (thiourea) at the beginning of the synthesis process

(in situ doping process) can yield CDPM-TiO_2 with higher activity than the ex situ doping process. The highest photocatalytic activity of CDPM300 can be attributed to the higher adsorption capacity (higher surface area, smaller particle size and larger pore volume), higher dopants content, more intra photoactive centers and catalytic active surface sites, as well as better polymorphic ratio. This study on the S, N and C co-doped polymorphic titanium dioxide nanoparticles not only provides fundamental data for the properties of co-doped polymorphic TiO_2 nanoparticles but can also be considered as a promising demonstration of such visible light-sensitized photocatalysts in environmental applications, specifically for the treatment of cyanotoxin-contaminated water.

Disclaimer

The U.S. Environmental Protection Agency, through its Office of Research and Development, funded and managed, or partially funded and collaborated in, the research described herein. It has been subjected to the Agency's peer and administrative review and has been approved for external publication. Any opinions expressed are those of the author(s) and do not necessarily reflect the views of the Agency, therefore, no official endorsement should be inferred. Any mention of trade names or commercial products does not constitute endorsement or recommendation for use.

Acknowledgements

This US-Egypt collaborative work is funded by U.S. Department of Agriculture (58-3148-1-152). We are thankful to China Scholarship Council (CSC) Scholarships (2009617129) for the partially financial support.

References

[1] M.G. Antoniou, P.A. Nicolaou, J.A. Shoemaker, A.A. de la Cruz, D.D. Dionysiou, Applied Catalysis B: Environmental 91 (2009) 165–173.
[2] J. Zhang, J.P. Lei, C.L. Xu, L. Ding, H.X. Ju, Analytical Chemistry 82 (2010) 1117–1122.
[3] Y.F. Fang, Y.P. Huang, J. Yang, P. Wang, G.W. Cheng, Environmental Science & Technology 45 (2011) 1593–1600.
[4] W.H. Organization, Guidelines for Drinking-Water Quality, 4th ed., W.H. Organization, 2011.
[5] B.J.P.A. Cornish, L.A. Lawton, P.K.J. Robertson, Applied Catalysis B: Environmental 25 (2000) 59–67.
[6] R. Nishiwakimatsushima, T. Ohta, S. Nishiwaki, M. Suganuma, K. Kohyama, T. Ishikawa, W.W. Carmichael, H. Fujiki, Journal of Cancer Research and Clinical Oncology 118 (1992) 420–424.
[7] N.Q. Gan, X.Y. Sun, L.R. Song, Chemical Research in Toxicology 23 (2010) 1477–1484.
[8] R.A. Halvorson, P.J. Vikesland, Environmental Science & Technology 45 (2011) 5644–5651.
[9] M.G. Antoniou, A.A. de la Cruz, D.D. Dionysiou, Applied Catalysis B: Environmental 96 (2010) 290–298.
[10] P.K.J. Robertson, D.W. Bahnemann, L.A. Lawton, E. Bellu, Applied Catalysis B: Environmental 108 (2011) 1–5.
[11] I. Liu, L.A. Lawton, D.W. Bahnemann, P.K.J. Robertson, Applied Catalysis B: Environmental 60 (2005) 245–252.
[12] A.J. Feitz, T.D. Waite, G.J. Jones, B.H. Boyden, P.T. Orr, Environmental Science & Technology 33 (1999) 243–249.
[13] P. Chowdhury, J. Moreira, H. Gomaa, A.K. Ray, Industrial & Engineering Chemistry Research 51 (2012) 4523–4532.
[14] E. Bae, W. Choi, Environmental Science & Technology 37 (2003) 147–152.
[15] J. Choi, H. Park, M.R. Hoffmann, Journal of Physical Chemistry C 114 (2010) 783–792.
[16] M. Pelaez, A.A. de la Cruz, E. Stathatos, P. Falaras, D.D. Dionysiou, Catalysis Today 144 (2009) 19–25.
[17] G.L. Liu, C. Han, M. Pelaez, D.W. Zhu, S.J. Liao, V. Likodimos, N. Ioannidis, A.G. Kontos, P. Falaras, P.S.M. Dunlop, J.A. Byrne, D.D. Dionysiou, Nanotechnology 23 (2012) 294003.
[18] C. Han, M. Pelaez, V. Likodimos, A.G. Kontos, P. Falaras, K. O'Shea, D.D. Dionysiou, Applied Catalysis B: Environmental 107 (2011) 77–87.
[19] Y.C. Zhang, M. Yang, G. Zhang, D.D. Dionysiou, Applied Catalysis B: Environmental 142–143 (2013) 249–258.
[20] G. Barolo, S. Livraghi, M. Chiesa, M.C. Paganini, E. Giamello, Journal of Physical Chemistry C 116 (2012) 20887–20894.
[21] C. Di Valentin, E. Finazzi, G. Pacchioni, A. Selloni, S. Livraghi, M.C. Paganini, E. Giamello, Chemical Physics 339 (2007) 44–56.
[22] J.C. Yu, W.K. Ho, J.G. Yu, H. Yip, P.K. Wong, J.C. Zhao, Environmental Science & Technology 39 (2005) 1175–1179.
[23] T. Tachikawa, S. Tojo, K. Kawai, M. Endo, M. Fujitsuka, T. Ohno, K. Nishijima, Z. Miyamoto, T. Majima, Journal of Physical Chemistry B 108 (2004) 19299–19306.
[24] C. Di Valentin, G. Pacchioni, A. Selloni, Chemistry of Materials 17 (2005) 6656–6665.
[25] J.A. Rengifo-Herrera, E. Mielczarski, J. Mielczarski, N.C. Castillo, J. Kiwi, C. Pulgarin, Applied Catalysis B: Environmental 84 (2008) 448–456.
[26] D.C. Hurum, A.G. Agrios, K.A. Gray, T. Rajh, M.C. Thurnauer, Journal of Physical Chemistry B 107 (2003) 4545–4549.
[27] F. Dong, W.R. Zhao, Z.B. Wu, Nanotechnology 19 (2008) 365607.
[28] N.D. Feng, A.M. Zheng, Q.A. Wang, P.P. Ren, X.Z. Gao, S.B. Liu, Z.R. Shen, T.H. Chen, F. Deng, Journal of Physical Chemistry C 115 (2011) 2709–2719.
[29] S. Kaewgun, D. Mckinney, J. White, A. Smith, M. Tinker, J. Ziska, B.I. Lee, Journal of Photochemistry and Photobiology A: Chemistry 202 (2009) 154–158.
[30] S. Kaewgun, B.I. Lee, Journal of Photochemistry and Photobiology A: Chemistry 210 (2010) 162–167.
[31] B.I. Lee, X.Y. Wang, R. Bhave, M. Hu, Materials Letters 60 (2006) 1179–1183.
[32] R.C. Bhave, B.I. Lee, Materials Science and Engineering A: Structural Materials Properties Microstructure and Processing 467 (2007) 146–149.
[33] X.X. He, M. Pelaez, J.A. Westrick, K.E. O'Shea, A. Hiskia, T. Triantis, T. Kaloudis, M.I. Stefan, A.A. de la Cruz, D.D. Dionysiou, Water Research 46 (2012) 1501–1510.
[34] H.Z. Zhang, J.F. Banfield, Journal of Physical Chemistry B 104 (2000) 3481–3487.
[35] P. Periyat, S.C. Pillai, D.E. McCormack, J. Colreavy, S.J. Hinder, Journal of Physical Chemistry C 112 (2008) 7644–7652.
[36] J. Striova, C. Lofrumento, A. Zoppi, E.M. Castellucci, Journal of Raman Spectroscopy 37 (2006) 1139–1145.
[37] S. Triebold, G.L. Luvizotto, R. Tolosana-Delgado, T. Zack, H. von Eynatten, Contributions to Mineralogy and Petrology 161 (2011) 581–596.
[38] G.A. Tompsett, G.A. Bowmaker, R.P. Cooney, J.B. Metson, K.A. Rodgers, J.M. Seakins, Journal of Raman Spectroscopy 26 (1995) 57–62.
[39] S. Balaji, Y. Djaoued, J. Robichaud, Journal of Raman Spectroscopy 37 (2006) 1416–1422.
[40] A. Li Bassi, D. Cattaneo, V. Russo, C.E. Bottani, E. Barborini, T. Mazza, P. Piseri, P. Milani, F.O. Ernst, K. Wegner, S.E. Pratsinis, Journal of Applied Physics 98 (2005) 074305.
[41] D. Bersani, P.P. Lottici, X.Z. Ding, Applied Physics Letters 72 (1998) 73–75.
[42] T. Ohno, M. Akiyoshi, T. Umebayashi, K. Asai, T. Mitsui, M. Matsumura, Applied Catalysis A: General 265 (2004) 115–121.
[43] Y.X. Li, C.F. Xie, S.Q. Peng, G.W. Lu, S.B. Li, Journal of Molecular Catalysis A: Chemical 282 (2008) 117–123.
[44] T. Matsumoto, N. Iyi, Y. Kaneko, K. Kitamura, S. Ishihara, Y. Takasu, Y. Murakami, Catalysis Today 120 (2007) 226–232.
[45] S. Sakthivel, M. Janczarek, H. Kisch, Journal of Physical Chemistry B 108 (2004) 19384–19387.
[46] H. Lin, C.P. Huang, W. Li, C. Ni, S.I. Shah, Y.H. Tseng, Applied Catalysis B: Environmental 68 (2006) 1–11.
[47] M. Nasir, Z.H. Xi, M.Y. Xing, J.L. Zhang, F. Chen, B.Z. Tian, S. Bagwasi, Journal of Physical Chemistry C 117 (2013) 9520–9528.
[48] B. Naik, K.M. Parida, C.S. Gopinath, Journal of Physical Chemistry C 114 (2010) 19473–19482.
[49] J.A. Rengifo-Herrera, K. Pierzchala, A. Sienkiewicz, L. Forro, J. Kiwi, J.E. Moser, C. Pulgarin, Journal of Physical Chemistry C 114 (2010) 2717–2723.
[50] W.J. Ren, Z.H. Ai, F.L. Jia, L.Z. Zhang, X.X. Fan, Z.G. Zou, Applied Catalysis B: Environmental 69 (2007) 138–144.
[51] K.L. Tan, L.L. Woon, H.K. Wong, E.T. Kang, K.G. Neoh, Macromolecules 26 (1993) 2832–2836.
[52] D.M. Chen, Z.Y. Jiang, J.Q. Geng, Q. Wang, D. Yang, Industrial & Engineering Chemistry Research 46 (2007) 2741–2746.
[53] H.B. Liu, Y.M. Wu, J.L. Zhang, ACS Applied Materials & Interfaces 3 (2011) 1757–1764.
[54] H.Q. Wang, Z.B. Wu, Y. Liu, Journal of Physical Chemistry C 113 (2009) 13317–13324.
[55] V. Kiran, S. Sampath, ACS Applied Materials & Interfaces 4 (2012) 3818–3828.
[56] H.X. Li, X.Y. Zhang, Y.N. Huo, J. Zhu, Environmental Science & Technology 41 (2007) 4410–4414.
[57] S.X. Liu, X.Y. Chen, Journal of Hazardous Materials 152 (2008) 48–55.
[58] H.Q. Sun, Y. Bai, H.J. Liu, W.Q. Jin, N.P. Xu, G.J. Chen, B.Q. Xu, Journal of Physical Chemistry C 112 (2008) 13304–13309.
[59] G.M. Underwood, T.M. Miller, V.H. Grassian, Journal of Physical Chemistry A 103 (1999) 6184–6190.
[60] J. Madarasz, A. Braileanu, M. Crisan, G. Pokol, Journal of Analytical and Applied Pyrolysis 85 (2009) 549–556.
[61] Y. Kuroda, T. Mori, K. Yagi, N. Makihata, Y. Kawahara, M. Nagao, S. Kittaka, Langmuir 21 (2005) 8026–8034.
[62] J.L. Ropero-Vega, A. Aldana-Perez, R. Gomez, M.E. Nino-Gomez, Applied Catalysis A: General 379 (2010) 24–29.
[63] H. Xu, L.Z. Zhang, Journal of Physical Chemistry C 113 (2009) 1785–1790.
[64] J.C. Yu, L.Z. Zhang, J.G. Yu, Chemistry of Materials 14 (2002) 4647–4653.
[65] Y.C. Zhang, J. Li, H.Y. Xu, Applied Catalysis B: Environmental 123 (2012) 18–26.
[66] S.J. Ding, X. Yin, X.J. Lu, Y.M. Wang, F.Q. Huang, D.Y. Wan, ACS Applied Materials & Interfaces 4 (2012) 306–311.